DEMONSTRATION OF FABRY-PEROT INTERFEROMETRY FOR PHOTOLITHOGRAPHY MASKS

Md Iftekharul Islam[1,2], Amrid Amnache[1,2], Richard Beaudry[3], Maurice Delafosse[3], Serge Ecoffey[1,2], and Luc G. Fréchette[1,2]*

[1]Institut Interdisciplinaire d'Innovation Technologique (3IT), Université de Sherbrooke, Sherbrooke, Canada
[2]Laboratoire Nanotechnologies et Nanosystèmes (LN2), CNRS UMI-3463, Université de Sherbrooke, Sherbrooke, Canada
[3]Digitho Technologies Inc., Bromont, Québec, Canada

ABSTRACT

A Fabry-Perot Pixel aimed for adaptive photolithography is successfully fabricated and demonstrated. To the authors' knowledge, this is the first use of Fabry-Perot interferometry for optical photomasks. Pixels, both transmissive and opaque to ultraviolet light, were shown to control the exposure dose of a photoresist. On and off states were achieved for 350 nm and 310 nm air gap, respectively, corresponding to a transmission contrast over 50%. Once the pixels become actionable, arrays of these MEMS pixels covering a photomask will allow a programmable mask that can be used in conventional photolithography tools.

KEYWORDS

Fabry-Perot Pixel, Interference, Adaptive Photomask, Photolithography, Light Transmission, MEMS.

INTRODUCTION

A conventional photolithography system utilizes a photomask to create patterns in the photoresist layer beneath it. The mask typically consists of a transparent material, such as glass, with an opaque film coating, usually made of chromium (Cr), containing patterns. The Cr blocks optical flow, while the areas without it permit light to enter the photosensitive layer for pattern transfer. As these patterns are permanent, a distinct mask is required for each layout. New patterns or corrections require the fabrication of new masks, which incurs cost and delays. Therefore, there is a need for a flexible mask system that can be utilized multiple times.

Programmable photolithography masks offer such flexibility and efficiency in patterning integrated circuits. Unlike traditional photomasks, these programmable masks use dynamic lithography techniques, which enables rapid prototyping and customization of chip designs. Recent advancements in digital micromirror devices (DMDs) [1] and liquid crystal displays (LCDs) [2] have enhanced the resolution, speed, and versatility of programmable photomasks. These devices utilize arrays of individually controllable elements to modulate light waves, which facilitates real-time adjustments to accommodate diverse circuit designs and process nodes. However, optical properties of LCDs vary greatly with temperature [3]. Hence, temperature control on the portable device is difficult. Additionally, liquid crystals are organic compounds that degrades with ultraviolet (UV) light [4]. This can lead to fast degradation of the photomask which can cause lithography process variations and high replacement rate. On the other hand, DMDs usually have binary states of on and off [5]. This prevents it being used for grayscale imaging. To provide grayscale images, it requires selective tilting of mirrors, which affects telecentric behavior of the mirror as it is no longer perpendicular to the image plane [5]. Using telecentric illumination ensures improved uniformity of light distribution across the DMD and minimizes distortion in the illumination by reducing the illumination angle. Moreover, these mask technologies either propose a new photolithography system or require a significant upgrade of the conventional ones to integrate them.

The proposed programmable photomask [6] will offer a customizable option for accommodating multiple patterns using a single mask. The adaptive mask will be adaptable to traditional masks of similar dimensions used in high-volume manufacturing (HVM) machines, requiring less modification in the stepper photolithography systems for seamless integration. The mask will consist of an array of actionable MEMS pixels, each using Fabry-Perot (FP) interference to reflect or transmit light. A pixel consists of a cavity formed between a substrate and a movable membrane. By using constructive and destructive interferences, the pixel can become transparent or opaque for light waves traveling in the system. The objective of this paper is to demonstrate the proof of concept of FP effect on the photo-sensitive resist using the novel Fabry-Perot Pixel (FPP) device.

FABRY-PEROT PIXEL PRINCIPLE

Since the invention of Fabry-Perot Interferometer (FPI) by Charles Fabry and Alfred Perot in 1899, the principle has been a widely recognized term in optics. The most common form of FPI comprises two parallel, semi-transparent, and highly reflective surfaces with a narrow gap in between [7]. The refractive index of these layers is typically higher than the refractive index of the air gap in between. The advancements in materials science, fabrication techniques, and signal processing have boosted FPI's versatility and efficacy over the years. Prominent applications include high-resolution spectroscopy [8], optical sensing [9], and biomedical imaging [10]. These applications highlight FPI's ability to address a wide range of technological challenges across different domains. However, this is the first time the FP concept is used in the domain of photolithography masks, to the authors' knowledge.

The FPP and its interference conditions are illustrated in Figure 1. A light wave enters the first material layer, passes through the air gap to the second layer. Together, the layers and the air gap form an optical cavity. When the light reaches the second reflecting surface, a portion of it is transmitted, and the remainder is reflected. The reflected wave continues the process and generates another transmitted wave. All these transmitted waves interact with each other and can be in-phase or out-of-phase depending on the path difference between them. As demonstrated in Figure 1 (b), the transmission is at a minimum when the transmitted light experiences destructive interference, under the following specific condition [7]:

$$\Phi = (2n+1)\,\pi \tag{1}$$

where, Φ is the phase difference between the adjacent transmitted waves, and n is an integer.

When the transmission is minimum, most of the light is reflected, preventing light transmission at a specific wavelength. This is the reflective FP situation which corresponds to the off-state of the pixel. By modifying the optical path, i.e., air gap, the interference condition can be changed to constructive, which results in maximum transmission. Figure 1 (c) illustrates this maximum transmission state, where the transmitted light experiences constructive interference based on the below criteria:

$$\Phi = 2n\pi \tag{2}$$

This allows light transmission in the transmissive FP state, resulting in the on-state of the pixel.

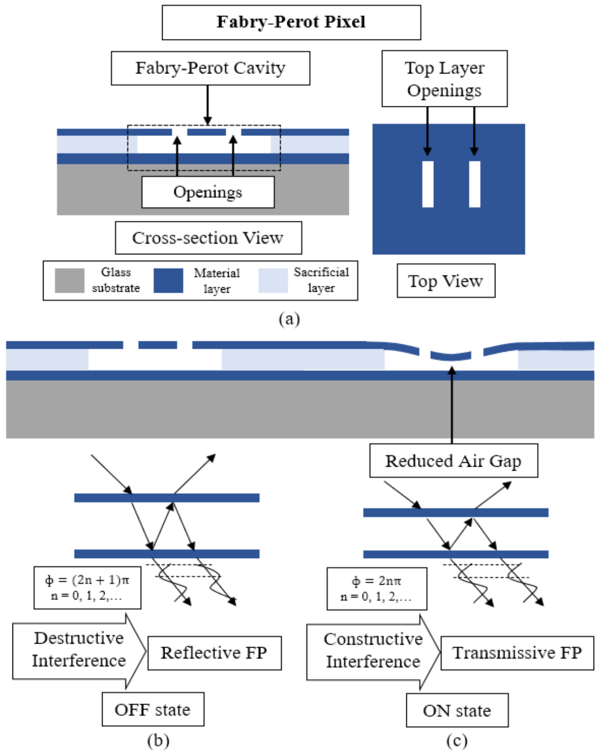

Figure 1: Representation of the (a) Fabry-Perot Pixel and its operating condition in the (b) destructive and (c) constructive interference modes.

The wave properties of light determine that the patterning resolution is limited to a certain fraction of the wavelength. According to Raleigh criterion, this minimum resolution density, d_{res}, can be expressed by [11],

$$d_{res} = \frac{K_1 \lambda}{NA} \tag{3}$$

where, K_1 is the Raleigh coefficient that represents the effect of photoresist abilities, irradiation condition, and photomask technology, λ is the exposure wavelength, and NA is the numerical aperture of the lens system, which is defined as,

$$NA = n \sin \theta \tag{4}$$

where, n is the refractive index of the medium adjacent to the photoresist, and θ is the incident angle on the resist. The novel FPP mask is designed to work in 365 nm (i-line lithography) wavelength. So from eq. 3, the minimum resolution that can be reached is 220 nm with K_1= 0.60 and NA = 0.65 [12].

DESIGN METHODOLOGY

The mechanical and optical properties of low-stress silicon nitride (Si_xN_y) make it highly suitable for fabricating tunable FPIs [13] [14]. It allows the fabrication of large-area membranes (>10 mm) with extreme flatness [13]. Additionally, Si_xN_y exhibits a refractive index nonuniformity of less than 10^{-4} and optical absorption losses below 0.5% for UV range between 280-400 nm [13]. Plasma-enhanced chemical vapor deposition (PECVD) is widely used for Si_xN_y deposition in lower temperature (~300 °C) for temperature sensitive device process flow [14]. By using these electro-optic properties of Si_xN_y, the FPIs can dynamically adjust their optical properties, such as resonance wavelength and finesse, making them ideal candidates for optical filters, switches, and sensors [15].

Upon selecting Si_xN_y as the structural material for the FPP, transmittance simulations were performed using Filmetrics' spectral reflectance calculator [16]. This online calculator utilizes the complex-matrix form of Fresnel equations to derive results. The material layers along with their respective thicknesses used for the simulation are specified in Table 1. For given Si_xN_y thicknesses of 320 nm and 50 nm, the off-state transmittance was observed to be 36% at an air gap of 370 nm, while the on-state transmittance reached 92% at an air gap of 290 nm, for a specific wavelength of 365 nm, as shown in Figure 2. A variation of ±10 nm in air gap contributes to transmission percentage difference of less than 7%.

Table 1: Layer properties for transmittance simulation.

Layer	Material	Thickness
1	Quartz	500 µm
2	Si_xN_y	320 nm
3	Air	290/370 nm
4	Si_xN_y	50 nm

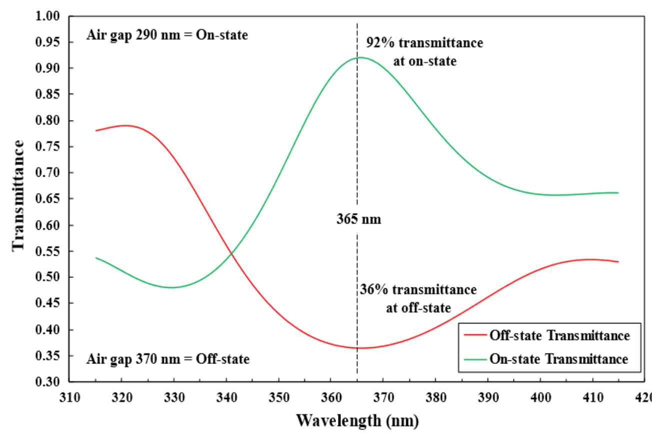

Figure 2: Transmittance curve in the off-state and on-state conditions for the thin film stack (includes two silicon nitride layers and an air gap in between) used to simulate the Fabry-Perot Pixel (derived from the Filmetrics' spectral reflectance calculator [16]).

MICROFABRICATION PROCESS FLOW

To demonstrate the FP principle, a functional FPP was fabricated on a 500 µm thick quartz substrate, with different values of fixed air gap. The fabrication steps are illustrated in Figure 3. A 320 nm low-stress Si_xN_y layer was deposited using PECVD, which serves as the bottom transparent layer of the FPP. A mixed frequency recipe combining both high-frequency (HF) and low-frequency (LF) cycle was utilized for this deposition. HF (13.5 MHz) and LF (380 kHz) power were set to 30 W and 22 W, respectively, and chamber pressure to 900 mTorr. The gas flow rates were as follows: SiH_4 40 sccm, NH_3 55 sccm, and N_2 1960 sccm, while maintaining a deposition temperature of 300 °C. Following this, an a-Si layer was deposited via PECVD, acting as the sacrificial layer. Power was set to 55 W and chamber pressure to 550 mTorr, with gas flow rates of SiH_4 58 sccm, and Ar 500 sccm, at a deposition temperature of 300 °C. The a-Si layer defined the air gap between the top and bottom Si_xN_y layers. Subsequently, the top PECVD Si_xN_y layer was deposited. A 50 nm low-stress layer was deposited using the same recipe as the bottom Si_xN_y deposition. The PECVD depositions were carried out using a STS MESC Multiplex PECVD machine. A total of six FPP devices with various a-Si thicknesses were fabricated. The thickness of a-Si layer was varied from 270 nm to 370 nm with a 20 nm step to adjust the air gap of the FPP cavity to observe constructive and destructive interferences.

A photolithography process was then carried out to define the openings in the top layer. Positive AZ 1512 photoresist (1.2 µm) was employed for patterning, and AZ 300 MIF served as the developer. The exposure was done on an OAI 806 mask aligner. After that, an SF_6 plasma was carried out in an STS Multiplex Inductively Coupled (ICP) plasma machine to etch Si_xN_y and a-Si and reach the bottom Si_xN_y layer. Si_xN_y was etched using a higher platen power recipe, whereas a lower platen power (selective to Si_xN_y) was used to etch a-Si isotropically and release the membrane. Finally, the resist was removed through O_2 plasma. The openings in the top layer (Figure 3 (c)) are required to etch the sacrificial layer and will allow light transmission regardless of the air gap. However, the area between and around the openings will transmit light or not depending on the air gap (defined by the sacrificial layer thickness).

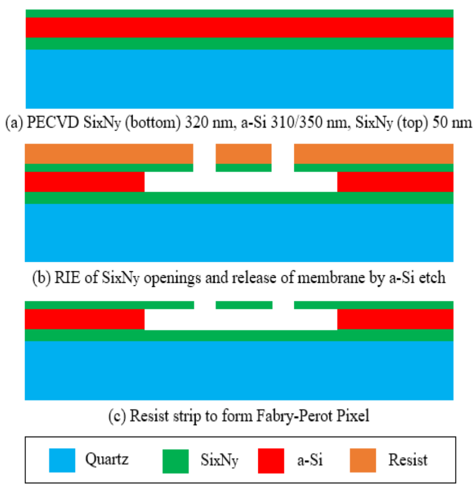

Figure 3: Fabrication steps of the Fabry-Perot Pixel (not to scale).

EXPERIMENTS AND RESULTS

Prior testing the FP efficiency, an exposure dose matrix was performed to evaluate the minimum UV dose, named energy zero or E_o, necessary for full development of the resist. Below this exposure dose, the photoresist is under exposed, and some thickness of the resist will remain. Above this level, the exposed resist is fully dissolved in the developer. A quartz substrate was used to spin coat 500 nm of AZ 1505 photoresist. The ellipsometer was used to measure the resist thickness before and after exposure and development. Energy doses from 50 mJ.cm^{-2} to 200 mJ.cm^{-2} were used to expose the resist on the substrate.

Table 2: Development on photoresist with various exposure dose.

Exposure Dose (mJ.cm^{-2})	Development on Photoresist
50	Underdeveloped
100	Underdeveloped
120	Underdeveloped
150	Fully Developed
200	Fully Developed

Table 2 summarizes the results of various exposure dose on the photoresist. Based on resist development, E_o was therefore between 120 mJ.cm^{-2} and 150 mJ.cm^{-2}. 135 mJ.cm^{-2} was set to be the nominal value of E_o.

While using FPP as the photomask, the transmitted energy to the photoresist depends on the transmittance of the FPP and it can be determined with the equation below:

$$E = DT \quad (5)$$

where D is the exposure dose and T is the transmittance of the FPP.

The exposure dose must be chosen such that $E > E_o$ for the on state of the FPP and $E < E_o$ for the off state of it. The exposure dose with FPP was therefore chosen to be 200 mJ.cm^{-2}, which is about 1.5 times of E_o. Using eq. 5 and the simulated transmittance value from earlier, transmitted energy at off state was 72 mJ.cm^{-2} (0.5E_o) and at on state was 184 mJ.cm^{-2} (1.3E_o).

The FPP was tested using a dedicated experimental setup, as depicted in Figure 4. First, a quartz substrate was coated with 1.2 µm of AZ 1512 photoresist. The FPP was then placed face-to-face with the quartz substrate so that the top Si_xN_y layer was directly in contact with the photo-sensitive resist. An OAI 806 mask aligner was used for the UV exposure in hard contact mode. A 365 nm filter was used during operation with the aforementioned exposure dose of 200 mJ.cm^{-2}.

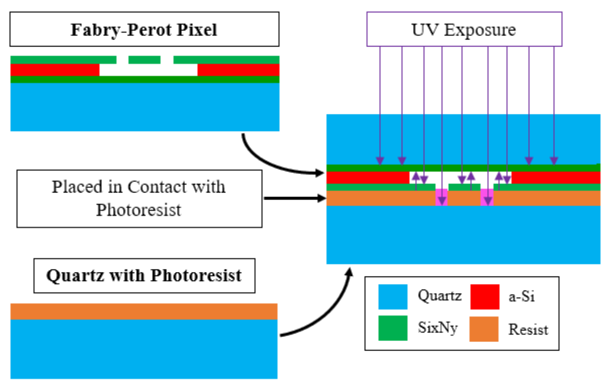

Figure 4: Schematic view of the experimental setup of the Fabry-Perot Pixel (illustrated in reflective mode).

The resulting effects on the photoresist under the reflective and transmissive FP conditions are shown in Figure 5. Destructive (reflective FP) and constructive (transmissive FP) interferences were achieved with FPP having 350 nm and 310 nm air gap, respectively. The difference in air gap from transmittance simulation at which the interferences occur is due to the change of the gap thickness from stress in the top Si_xN_y layer of FPP (Figure 5 (a)) after release. As a result, there is a shift in the maximum and minimum positions of FP interference conditions.

In the reflective FP situation, the photosensitive resist was underdeveloped due to partial light transmission between and around the openings as illustrated in Figure 5 (b). With constructive interference in transmissive FP condition, the light was transmitted through the FPP layers and openings, and the resist was exposed over the entire designated area as observed in Figure 5 (c). The variation of shape is explained by the difference in distance between the openings. When the distance is small, the FP effect around the openings overlaps more, thus creating a circular shape. The ellipsoidal structure is due to the larger gap (less overlapping) between the openings.

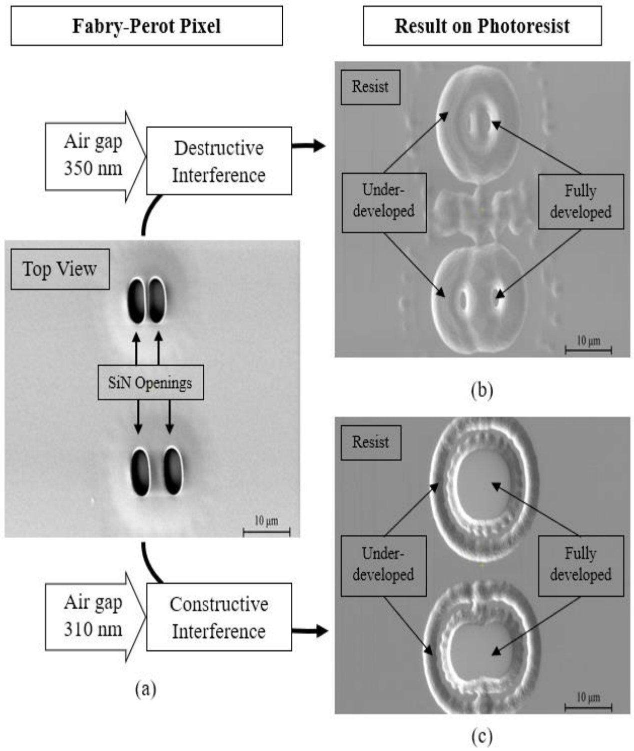

Figure 5: SEM images of the results of the (a) Fabry-Perot Pixel on photoresist for the (b) reflective FP, where only the photoresist through the openings is fully developed, and the (c) transmissive FP, where the entire zone of the FP cavity is fully developed. This demonstrates exposure dose control using FP interferometry for the first time.

The subsequent step is to incorporate a MEMS device that can actuate and control the air gap (cavity) of the FPPs on demand. With variable FPPs, it will become possible to adjust the air gap to various dimensions. This will result in the attainment of the highest or lowest level of light transmission, as well as any value in between. By utilizing electrostatic MEMS actuation of arrays of FPPs, a programmable photomask will be designed for 365 nm (i-line) photolithography systems.

CONCLUSION

The proof of concept of FP interferometry has shown to work in a UV photolithography system. FPPs with various fixed gaps were successfully fabricated using two Si_xN_y layers with an air gap in between. Destructive and constructive interferences were achieved corresponding to the on and off states of the pixels, respectively, for different air gaps of FP cavities. This demonstrated the underlying FP principle for the development of a novel programmable photomask system that can be integrated into stepper photolithography tools.

ACKNOWLEDGEMENTS

The authors express their gratitude to Digitho Technologies Inc. and the Mitacs Business Strategy Internship (BSI) program for funding this research project. Support from the 3IT and LNN are greatly appreciated.

REFERENCES

[1] K. J. Zhong, Y. Q. Gao, and F. Li, “Maskless Lithography Based on DMD,” Key Eng. Mater., vol. 552, pp. 207–213, May 2013, doi: 10.4028/www.scientific.net/KEM.552.207.

[2] Y.-G. Ju, H.-J. Kim, and Y.-M. Ko, “Microscope projection photolithography based on liquid crystal microdisplay,” Eur. J. Phys., vol. 41, no. 5, p. 055301, Sep. 2020, doi: 10.1088/1361-6404/ab988f.

[3] J. Li, S. Gauza, and S.-T. Wu, “Temperature effect on liquid crystal refractive indices,” J. Appl. Phys., vol. 96, no. 1, pp. 19–24, Jul. 2004, doi: 10.1063/1.1757034.

[4] P.-T. Lin, S.-T. Wu, C.-Y. Chang, and C.-S. Hsu, “UV Stability of High Birefirngence Liquid Crystals,” Mol. Cryst. Liq. Cryst., vol. 411, no. 1, pp. 243–253, Jan. 2004, doi: 10.1080/15421400490435233.

[5] H. Sewell, “Maskless Optical Writer,” US-7012674-B2, Mar. 14, 2006 [Online]. Available: http://rb.gy/461ftk

[6] R. Beaudry, “Photolithography mask and photolithography system comprising said photolithography mask,” CA3184009C, Apr. 25, 2023 [Online]. Available: http://rb.gy/w6g2a0

[7] H. Van De Stadt and J. M. Muller, “Multimirror Fabry–Perot interferometers,” J. Opt. Soc. Am. A, vol. 2, no. 8, p. 1363, Aug. 1985, doi: 10.1364/JOSAA.2.001363.

[8] S. Ben-Ami, M. López-Morales, J. Garcia-Mejia, G. G. Abad, and A. Szentgyorgyi, “High-resolution Spectroscopy Using Fabry–Perot Interferometer Arrays: An Application to Searches for O2 in Exoplanetary Atmospheres,” Astrophys. J., vol. 861, no. 2, p. 79, Jul. 2018, doi: 10.3847/1538-4357/aac835.

[9] T. Zhang, Z. Gong, R. Giorno, and L. Que, “A nanostructured Fabry-Perot interferometer,” Opt. Express, vol. 18, no. 19, p. 20282, Sep. 2010, doi: 10.1364/OE.18.020282.

[10] X. Ma, M. Fan, Y. Cai, L. Xu, and J. Ma, “A Fabry–Perot Fiber-Optic Array for Photoacoustic Imaging,” IEEE Trans. Instrum. Meas., vol. 71, pp. 1–8, 2022, doi: 10.1109/TIM.2022.3147884.

[11] M. Rothschild, “Projection optical lithography,” Mater. Today, vol. 8, no. 2, pp. 18–24, Feb. 2005, doi: 10.1016/S1369-7021(05)00698-X.

[12] D. P. Sanders, “Advances in Patterning Materials for 193 nm Immersion Lithography,” Chem. Rev., vol. 110, no. 1, pp. 321–360, Jan. 2010, doi: 10.1021/cr900244n.

[13] J. H. Correia, M. Bartek, and R. F. Wolffenbuttel, “Bulk-micromachined tunable Fabry–Perot microinterferometer for the visible spectral range,” Sens. Actuators Phys., vol. 76, no. 1–3, pp. 191–196, Aug. 1999, doi: 10.1016/S0924-4247(99)00023-0.

[14] K. J. Winchester and J. M. Dell, “Tunable Fabry-Pérot cavities fabricated from PECVD silicon nitride employing zinc sulphide as the sacrificial layer,” J. Micromechanics Microengineering, vol. 11, no. 5, pp. 589–594, Sep. 2001, doi: 10.1088/0960-1317/11/5/323.

[15] H. Huang et al., “Determination of mechanical properties of PECVD silicon nitride thin films for tunable MEMS Fabry–Pérot optical filters,” J. Micromechanics Microengineering, vol. 15, no. 3, pp. 608–614, Mar. 2005, doi: 10.1088/0960-1317/15/3/024.

[16] “Spectral Thin Film Reflectance Calculator for Thin-Film Stacks.” Accessed: Jan. 15, 2024. [Online]. Available: https://www.filmetrics.com/reflectance-calculator

CONTACT

*Md Iftekharul Islam, Tel: +1-204-914-8695
md.iftekharul.islam@usherbrooke.ca